Slow photoelectron velocity-map imaging spectroscopy of the C_9H_7 (indenyl) and $C_{13}H_9$ (fluorenyl) anions

Jongjin B. Kim, Marissa L. Weichman, Tara I. Yacovitch,[a] Corey Shih, and Daniel M. Neumark[b]
Department of Chemistry, University of California, Berkeley, California 94720, USA
and Chemical Sciences Division, Lawrence Berkeley National Laboratory, Berkeley, California 94720, USA

(Received 3 June 2013; accepted 19 August 2013; published online 9 September 2013)

High-resolution photoelectron spectra are reported of the cryogenically cooled indenyl and fluorenyl anions, $C_9H_7^-$ and $C_{13}H_9^-$, obtained with slow electron velocity-map imaging. The spectra show well-resolved transitions to the neutral ground states, giving electron affinities of 1.8019(6) eV for indenyl and 1.8751(3) eV for fluorenyl. Numerous vibrations are observed and assigned for the first time in the radical ground states, including several transitions that are allowed only through vibronic coupling. The fluorenyl spectra can be interpreted with a Franck-Condon simulation, but explaining the indenyl spectra requires careful consideration of vibronic coupling and photodetachment threshold effects. Comparison of high- and low-resolution spectra along with measurements of photoelectron angular distributions provide further insights into the interplay between vibronic coupling and the photodetachment dynamics. Transitions to the neutral first excited states are also seen, with term energies of 0.95(5) eV and 1.257(4) eV for indenyl and fluorenyl, respectively. Those peaks are much wider than the experimental resolution, suggesting that nearby conical intersections must be considered to fully understand the vibronic structure of the neutral radicals. © *2013 AIP Publishing LLC*. [http://dx.doi.org/10.1063/1.4820138]

I. INTRODUCTION

Polycyclic aromatic hydrocarbons (PAHs) play a key role in diverse areas of chemistry. Incomplete combustion of fossil fuels leads to production of soot through aggregation of these species. Many PAHs are known to be mutagenic,[1] and their production is due to inefficient use of fuels, so considerable work has been put into understanding their properties and their formation pathways during combustion.[2,3] In the interstellar medium, although no particular PAH molecule has been definitively identified,[4] they are widely believed to be the carriers for various unidentified IR bands[5–7] and may contribute to the mysterious diffuse interstellar bands in the visible wavelengths.[8,9] However, mechanisms for the formation of interstellar PAHs are highly speculative. Possible contributions range from condensation similar to soot formation in terrestrial combustion[10] to fragmentation of carbon-rich grains.[11] Subsequent photochemistry and ion-molecule chemistry are also not well understood, but PAH decomposition may be a major source of the widely observed carbon chains and hydrocarbon radical species in space.[12,13]

The study of PAH species has focused almost exclusively on neutral closed-shell species with only cyclo-C_6 rings, but 5-member rings also play a key role in PAH chemistry. For example, one likely mechanism for the formation of fullerenes goes through growth of curved PAHs, which require 5-member rings.[14] The closed-shell molecules indene and fluorene are composed of one and two C_6 rings, respectively, fused to a cyclopentadiene moiety. These species have been characterized by many techniques, including photoelectron spectroscopy[15,16] and mass-analyzed threshold ionization spectroscopy.[17,18] In this paper, we focus on the deprotonated anion and neutral radical counterparts of these molecules, C_9H_7 (indenyl) and $C_{13}H_9$ (fluorenyl), shown in Fig. 1.

Indene, fluorene, and their dehydrogenated radical species have been implicated as important intermediates in combustion. Various thermochemical and kinetic calculations have predicted the formation of indene or indenyl by acetylene addition to fulvenallene,[19] cyclopentadienyl radical,[20] and benzyl radical.[21,22] Other proposed mechanisms include the addition of propargyl to benzyne,[23] as well as the oxidation of naphthyl radical followed by decomposition to indenyl.[24,25] Indenyl has also been identified as a product when acetylene is passed over nano-sized silicate particles.[26]

A computational study by Schaefer and co-workers[27] suggested that phenyl radical would react with C_3H_x species to form indene. Crossed molecular beam experiments by Kaiser and co-workers[28] confirmed the formation of indene from single collisions of deuterated phenyl radical with propyne and allene. Using photoionization to monitor the products in a high-temperature chemical reactor, this group also saw formation of indene under more combustion-relevant conditions with higher pressures and temperatures.[29] Similarly, Shukla *et al*. sampled the products of toluene pyrolysis in the presence of acetylene, and saw formation of indene, fluorene, and their corresponding dehydrogenated radicals.[30,31] These results were compared with calculations which

[a] Present address: Aerodyne Research, Billerica, Massachusetts 01821, USA.
[b] Author to whom correspondence should be addressed. Electronic mail: dneumark@berkeley.edu

 © 2013 AIP Publishing LLC

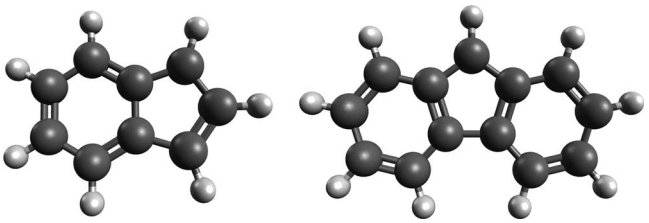

FIG. 1. Structures of indenyl (left) and fluorenyl (right).

suggested major indene formation through acetylene addition to benzyl radical, and fluorene formation through phenyl recombination with benzyl and subsequent cyclization.[32] Fluorenyl formation has also been predicted to form through acetylene addition to the indenyl radical.[33] Subsequent ring growth mechanisms have been proposed, but have not been investigated in as much detail.[2,24,31]

In spite of their chemical importance, the spectroscopy of the indenyl and fluorenyl radicals remains largely unexplored. ESR spectra have been measured for both radicals in solution.[34,35] Fischer and co-workers characterized the indenyl[36] and fluorenyl[37] radicals and their cations by threshold photoionization spectroscopy. In an inert gas matrix, visible absorption and emission of indenyl have been observed but not assigned,[38] while a combined Raman, FTIR, and UV/Vis study was carried out on fluorenyl.[39] However, no gas-phase data on the vibrational frequencies or excited state energies are available for the radicals. To our knowledge, the only gas-phase spectroscopic characterization of the indenyl and fluorenyl anions is from electron photodetachment cross sections measured by Römer *et al.*, who found electron affinities of 1.853(14) and 1.864(14) eV for the respective neutral radicals.[40]

The indenyl and fluorenyl anions are closed-shell aromatic species. As demonstrated by Lineberger and coworkers[41–43] for cyclopentadienide ($C_5H_5^-$) and other species, aromatic anions are relatively easy to generate, and anion photoelectron spectroscopy (PES) is a convenient tool for obtaining electron affinities, state energies, and vibrational structure of the neutral radicals. However, PES has a typical resolution of 80–100 cm^{-1}, which has limited its utility in obtaining vibrationally resolved spectra of complex systems with low-frequency modes or with several active modes.

Slow electron velocity-map imaging (SEVI) combined with cryogenic cooling of the anions can increase the resolution to 4 cm^{-1} for molecular systems.[44] In this paper, we report high-resolution SEVI spectra of cryo-cooled indenyl and fluorenyl anions. The improvements in resolution afforded by SEVI and ion cooling allow for vibrationally resolved spectra of these complex species even in the presence of significant spectral congestion. Vibrationally resolved transitions to the neutral ground electronic states are obtained. While much of the fluorenyl anion spectrum can be simulated by standard Franck-Condon analysis, many of the peaks observed in the indenyl spectrum are not Franck-Condon allowed, and appear to gain intensity through vibronic coupling to neutral excited states. The difference between the two species reflects a relatively unexplored relationship between vibronic coupling and the Wigner threshold law[45] for photodetachment cross sections. Photodetachment to the first excited states of both radicals is also observed, and the comparatively larger linewidths are suggestive of fast nonradiative decay to the ground state. Term energies and accurate electron affinities are obtained for both species. Assignments of the vibronic transitions are supported by electronic structure calculations, photoelectron angular distributions, and Franck-Condon simulations.

II. EXPERIMENTAL

The high-resolution SEVI spectrometer and the cryogenic ion trap have been described in detail previously.[44,46,47] SEVI uses a dispersive velocity-map imaging (VMI)[48] spectrometer to analyze the kinetic energy of electrons detached from anions of interest, optimized to collect slow electrons and thus achieve high energy resolution.

Indenyl and fluorenyl anions were formed by expanding dilute gas mixtures of indene and fluorene through an Even-Lavie pulsed molecular beam valve[49] equipped with a circular ionizer. The precursors indene and fluorene were stored in a cartridge heated to 40–70 °C. A gas mixture of trace NF_3 in 300 psi of He picked up the vapor and was expanded in vacuum. Electrons from the ionizer generated F^- by dissociative electron attachment to NF_3, which then deprotonated indene/fluorene, forming the anions of interest. The ions were guided to a radio-frequency ion trap held at 5 K, where they thermalized with a mix of cryogenic 20:80 H_2:He buffer gas for 40 ms. Under identical cooling conditions, we have measured an ion temperature of 10 K for C_5^-.[44] At this temperature, vibrational excitation of the anions should be negligible since the lowest frequency vibrations of the ions are expected to lie above 100 cm^{-1}.

The ions were then extracted into an orthogonal time-of-flight mass spectrometer. When mass-selected $C_9H_7^-$ or $C_{13}H_9^-$ ions reached the interaction region of the VMI spectrometer, they were photodetached with the output from a Nd:YAG-pumped tunable dye laser. The photoelectrons were focused with the VMI electrostatic lens onto an imaging detector, comprising a chevron-stacked pair of microchannel plates coupled to a phosphor screen and imaged with a CCD camera.[48] The key feature of the SEVI spectrometer is that relatively low voltages are applied to the VMI electron optics, resulting in a magnified image of the slow electrons and thus higher resolution than is typically obtained in VMI. Each frame was event-counted with centroiding to minimize noise and increase effective resolution.[50] The resulting images were used to reconstruct the original electron velocity distribution, using the inverse-Abel method of Hansen and Law,[51] and from this, the electron kinetic energy (eKE) distribution is obtained. By energy balance, the electron binding energy (eBE) is given by $eBE = h\nu - eKE$, where $h\nu$ is the photon energy.

Energy calibration was performed by acquiring SEVI spectra of O^- and Cl^-.[52,53] The spectrometer has a relatively constant resolving power $eKE/\Delta eKE$ and thus has better energy resolution with near-threshold (low-eKE) photoelectrons. Since the VMI stack also accelerates the electrons onto the imaging detector, the spectrometer is less susceptible to stray fields than a field-free time-of-flight detector, and

TABLE I. Peak positions, offsets from the origins, calculated positions, PADs, and assignments for the indenyl SEVI spectra. All energies are in cm^{-1}.

Peak	eBE	Offset	Calc. freq.	PAD	Assignment	Vib. sym.	Band
A	14 533	0	0	–	0_0^0	a_1	$\tilde{X}^2A_2 \leftarrow \tilde{X}^1A_1$
B	14 767	234		–			
C	15 053	520	523	–	26_0^1	b_1	
D	15 078	545	547	+	20_0^1	a_2	
E	15 099	567	568	–	41_0^1	b_2	
F	15 228	695	692	–	25_0^1	b_1	
G	15 257	724	726	+	19_0^1	a_2	
H	15 280	747	737	–	24_0^1	b_1	
I	15 320	787	784	+	18_0^1	a_2	
J	15 381	848	848	–	40_0^1	b_2	
K	15 402	869		–			
L	15 416	883		–			
M	15 462	929		–			
N	15 496	963		–			
O	15 517	984	995	–	39_0^1	b_2	
P	15 606	1073	1072	–	38_0^1	b_2	
Q	15 719	1186		–			
R	15 729	1196	1201	–	36_0^1	b_2	
S	15 838	1305		–			
T	15 891	1358	1359	–	34_0^1	b_2	
U	15 912	1379		–			
V	15 959	1426		–			
W	15 994	1461		–			
X	16 087	1554		–			
Y	16 116	1583		–			
A	22 200	0	0	–	0_0^0	a_1	$\tilde{A}^2B_1 \leftarrow \tilde{X}^1A_1$

thus maintains its resolving power very close to threshold. Typical peak widths with atomic systems are 5.3 cm^{-1} FWHM at 50 cm^{-1} above threshold; at only 13 cm^{-1} above threshold, peak widths narrow to 2.6 cm^{-1}. With the molecular systems here, typical FWHM peak widths were 6–9 cm^{-1} when taken 30–80 cm^{-1} above threshold. The additional width is likely due to the unresolved rotational profile under each vibronic transition. To obtain a full set of spectra, overview spectra of each electronic band were taken at intermediate resolution (~50 cm^{-1}). The laser frequency was then tuned in discrete steps to obtain a series of high-resolution spectra over a limited eKE range. Individual scans of this type were spliced together to form composite scans of the entire band; the intensity of each splice was scaled to the appropriate overview spectrum. As another basis for comparison, low-resolution (~200 cm^{-1}) scans were taken under settings that allowed for simultaneous observation of both electronic bands.

SEVI also yields the photoelectron angular distribution (PAD) for each photodetachment transition. For a one-photon process with light polarized parallel to the imaging plane, the PAD is given by the expression

$$I(\theta) = \frac{\sigma}{4\pi}\left(1 + \beta P_2(\cos\theta)\right), \quad (1)$$

where θ is the angle relative to the laser polarization axis and P_2 is the second-order Legendre polynomial.[54] The anisotropy parameter β varies from -1 to $+2$, corresponding to a PAD aligned perpendicular and parallel to the polarization axis, respectively. In general, the value of β varies with eKE and thus with the photon energy of a particular SEVI scan.[54–57] We did not carry out a comprehensive study of β vs. eKE, since many of the closely spaced peaks are not resolved at eKE > 200 cm^{-1}. Moreover, theoretical methods for predicting PADs for complex molecules are not yet in quantitative agreement with experiments.[58] Nevertheless, close to threshold, for a particular photodetachment transition, β is usually either consistently positive or negative to near-zero.[55] In Tables I and II (see below), peaks with $-1 \leq \beta \leq 0.1$ are labeled "–" and those with $0.2 \leq \beta \leq 2$ are labeled "+."

III. CALCULATIONS

The energetics, optimized geometries, and vibrational frequencies for all species were calculated with density functional theory (DFT), as it provides good balance between chemical accuracy and computational complexity. In particular, the B3LYP functional was used with the Pople-style 6-311+G* basis set. The maximum overlap method was used with B3LYP/6-311+G* for the excited states of the neutral species.[59] A state-averaged complete active space SCF (CASSCF) calculation with the 6-31+G* basis set was used to find the minimum energy conical intersection (MECI) between the ground and first excited states of the neutral radicals. The active space comprised 9 electrons in 9 π orbitals (9,9) for indenyl, and (13,13) for fluorenyl. The minima of the lowest two neutral states were also determined with CASSCF/6-31+G*, but not that of the anion, as dynamical

TABLE II. Peak positions, offsets from the origins, calculated positions, PADs, and assignments for the fluorenyl SEVI spectra. All energies are in cm^{-1}.

Peak	eBE	Offset	Calc. freq.	PAD	Assignment	Vib. sym.	Band
A	15 124	0	0	–	0_0^0	a_1	$\tilde{X}^2B_1 \leftarrow \tilde{X}^1A_1$
B	15 336	213	216	–	21_0^1	a_1	
C	15 418	294	296		39_0^1	b_1	
D	15 549	425	419	–	20_0^1	a_1	
E	15 653	529	526	+	37_0^1	b_1	
F	15 767	643	643	–	19_0^1	a_1	
G	15 818	694	687	+	36_0^1	b_1	
H	15 844	721		–			
I	15 863	739	738	–	18_0^1	a_1	
J	15 892	768		–			
K	15 902	779		–			
L	15 979	856	859	–	$19_0^1 21_0^1$	a_1	
M	15 987	864		–			
N	16 000	876	869	–	17_0^1	a_1	
O	16 055	932		–			
P	16 087	964		–			
Q	16 113	989		–			
R	16 216	1092	1096	–	15_0^1	a_1	
S	16 277	1153	1159	–	14_0^1	a_1	
T	16 306	1183		–			
U	16 327	1203		–			
V	16 371	1247	1246	–	12_0^1	a_1	
W	16 410	1286	1286	–	19_0^2	a_1	
X	16 479	1355		–			
Y	16 488	1364	1364	–	10_0^1	a_1	
Z	16 561	1437	1438	–	9_0^1	a_1	
AA	16 600	1477	1475	–	8_0^1	a_1	
AB	16 697	1574	1580	–	$10_0^1 21_0^1$	a_1	
AC	16 773	1649	1654	–	$9_0^1 21_0^1$	a_1	
A	25 254	0	0	–	0_0^0	a_1	$\tilde{A}^2A_2 \leftarrow \tilde{X}^1A_1$
B	25 685	430	436	–	20_0^1	a_1	
C	25 983	729	725	–	18_0^1	a_1	
D	26 153	899	873	–	20_0^2	a_1	
E	26 379	1125	1161	–	$18_0^1 20_0^1$	a_1	
F	26 777	1523	1509	–	9_0^1	a_1	

electron correlation must be included for accurate calculation of the electron affinity.[60]

Additional information on these and higher lying states was obtained from equation-of-motion ionization potential coupled-cluster (EOM-IP-CCSD) calculations using the closed-shell anion as a reference and a 6-31+G* basis set. This calculation yielded vertical detachment energies (VDE) to the lowest state of each irreducible representation in the neutral radicals that can be reached by one-electron detachment. EOM–IP–CCSD is expected to give qualitatively correct energies even in possibly multi-reference π-radical systems while still accounting for dynamical correlation.[61,62] Excited states of fluorenyl have been previously calculated in more detail with a combination of configuration interaction singles (CIS), time-dependent Hartree-Fock (TDHF), and time-dependent density functional theory (TDDFT).[63] Despite the different reference geometries and excitation methods, the corresponding excitation energies between the previous TDDFT results and our EOM-IP-CCSD results differ by less than 1 eV.

All DFT and EOM-IP-CCSD calculations were performed with Q-Chem 4.0,[64] and all CASSCF calculations were done with Molpro 2010.1.[65] All geometries converged to the C_{2v} structures shown in Fig. 1 for anionic and neutral C_9H_7 and $C_{13}H_9$. As recommended by Mulliken for planar C_{2v} molecules,[66] the x-axes were chosen to be perpendicular to the plane of the molecule; b_1 vibrational modes are out-of-plane and b_2 modes are in-plane.

Franck-Condon (FC) simulations were generated with the ezSpectrum program,[67] which takes geometries, frequencies, and normal modes for the anion and neutral states and generates the FC factors in the double-harmonic oscillator model, with full Duschinsky rotation of the normal modes.[68] All calculated frequencies were scaled by 0.98 for a best fit to the experimental results, and the positions of the 0_0^0 transitions were shifted to the positions of the experimentally assigned origins. As a test of the quantitative usefulness of calculated vibrational frequencies, the frequencies of benzene were computed at the same level of theory and compared to the most recent compilation of experimental results.[69] The

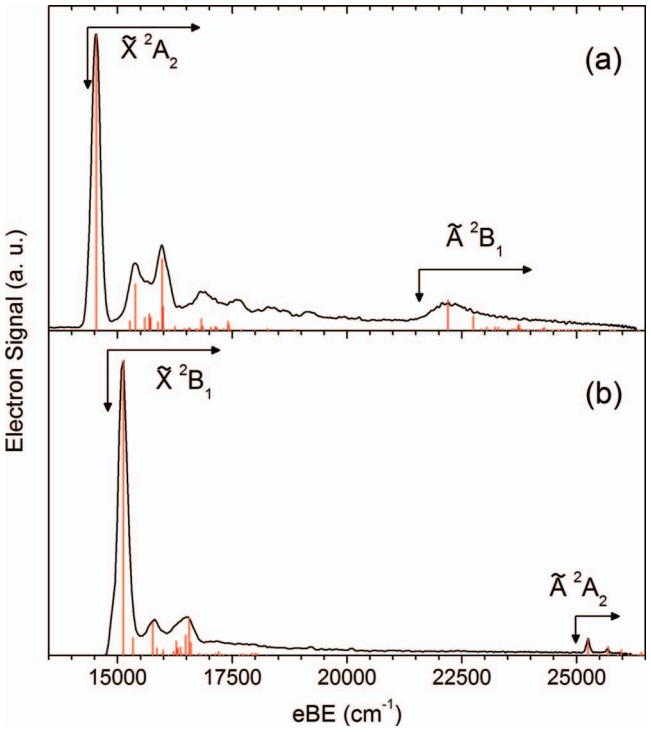

FIG. 2. Overview SEVI spectra of indenyl (panel (a)) and fluorenyl (panel (b)) showing detachment from the anions to the first two electronic states of the neutral radicals. Stick spectra (red) from FC simulations are displayed for comparison.

skeletal modes have a mean unsigned error of 5.9 cm^{-1}, suggesting that good agreement can be found between calculated and experimental peak positions in the aromatic systems studied here.

IV. RESULTS

Low-resolution photoelectron spectra of the indenyl and fluorenyl anions, each taken at a photon energy of 26 300 cm^{-1}, are shown in Fig. 2, with stick spectra of the simulated FC factors overlaid for comparison. Each spectrum shows an intense band with partially resolved structure between 14 500 and 19 000 cm^{-1} dominated by a single, well-separated peak at low eBE; the width of this peak is 230 cm^{-1} under these conditions. A weaker band is seen at higher eBE for both species. For each species, the two bands are assigned by inspection as transitions to the ground state and a low-lying excited electronic state of the neutral radical.

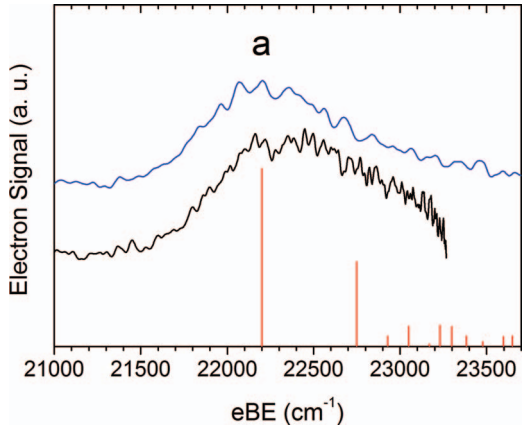

FIG. 4. SEVI spectra of photodetachment to the $\tilde{A}^2B_1$ excited state of indenyl. The upper blue trace is a low-resolution overview spectrum. The black lower trace is a spectrum taken at a lower photon energy with higher instrumental resolution for the band. The red stick spectrum is the FC simulation.

Higher-resolution spectra of the individual electronic bands are shown for indenyl in Figs. 3 and 4 and fluorenyl in Figs. 5 and 6. In Figs. 3 and 5, the uppermost green traces and red stick spectra are close-up views of the corresponding low-resolution spectra and FC simulations from Fig. 2. The middle blue traces, each showing a complete electronic band, are intermediate-resolution scans at lower photon energies of 16 153 cm^{-1} and 17 542 cm^{-1} in Figs. 3 and 5, respectively; these photon energies were chosen to cover the entire ground state band for each species. The black traces show high-resolution, low-eKE segments of SEVI spectra taken at discrete photon energies, spliced together and scaled to fit the intermediate-resolution scan. Typical peak widths in the black traces are 5–10 cm^{-1} FWHM in Figs. 3 and 5.

Figs. 4 and 6 highlight the higher-eBE bands of indenyl and fluorenyl. The red stick spectra are the same FC simulations shown in Fig. 2. The upper blue trace is an overview scan. For indenyl, this is just a section of the overview

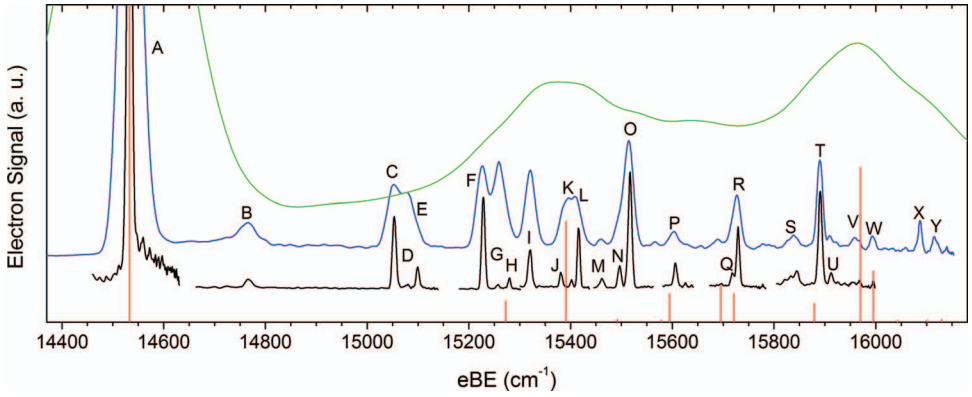

FIG. 3. SEVI spectra of photodetachment to the $\tilde{X}^2A_2$ ground state of indenyl. The upper green trace is a section of the low-resolution scan from Fig. 2(a). The middle blue trace is a higher resolution overview scan. The lower black traces are segments of high-resolution scans covering the range of the overview scan. The red stick spectrum is the FC simulation.

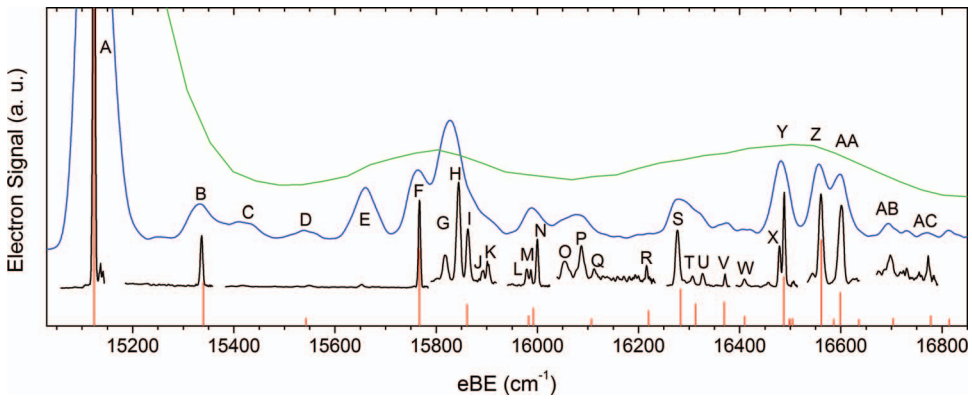

FIG. 5. SEVI spectra of photodetachment to the $\tilde{X}^2B_1$ ground state of fluorenyl. The upper green trace is the overview spectrum from Fig. 2(b). The middle blue trace is a higher resolution overview scan. The lower black traces are segments of high-resolution scans covering the range of the overview scan. The red stick spectrum is the FC simulation.

spectrum in Fig. 2(a). For fluorenyl, the blue trace was taken at a slightly higher photon energy of 28 575 cm^{-1} than in the overview scan owing to the limited energy window of the VMI spectrometer. The lower black traces are again segments of high-resolution scans, although only one such scan is shown for indenyl because no additional structure was seen under any circumstances. After accounting for instrumental resolution, the fluorenyl excited state has peak widths of 53 cm^{-1}, and the indenyl excited state band comprises a single peak with a width around 930 cm^{-1}. Peak positions, PADs, and assignments for the indenyl and fluorenyl SEVI spectra are summarized in Tables I and II.

As is evident in the overview scans in Fig. 2, each ground state band is dominated by a single major peak. Small peaks appear up to 2000 cm^{-1} above the major lowest eBE peak, but overall vibrational activity is minor. In Fig. 5, the peak intensities in the blue and black traces qualitatively follow the broad contours of the green overview spectrum. This does not appear to be the case for indenyl in Fig. 3, however. In addition, while almost every FC simulated peak for fluorenyl lines up with a high-resolution experimental peak, agreement between the simulated and high-resolution experimental spectra is notably poorer for indenyl. Tables I and II show that almost all peaks have PADs with negative-to-zero β, with the exception of peaks D, G, and I in indenyl and peaks E and G in fluorenyl. Comparison of the blue and black traces shows that the intensity of the "+" β peaks relative to the "−" β peaks generally drops off at low eKE.

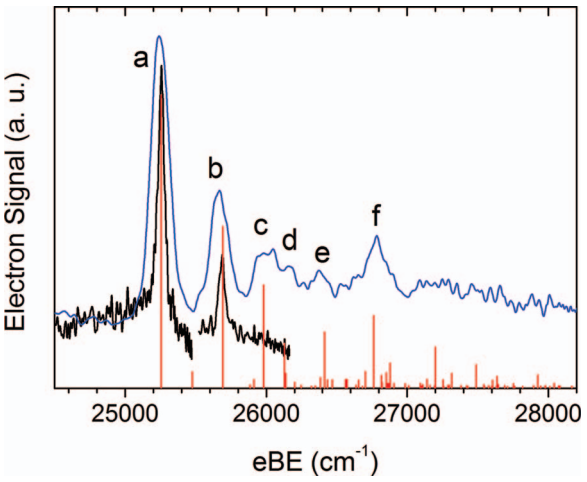

FIG. 6. SEVI spectra of photodetachment to the $\tilde{A}^2A_2$ excited state of fluorenyl. The upper blue trace is a low-resolution overview spectrum. The black lower traces are segments of high-resolution scans. The red stick spectrum is the FC simulation.

V. DISCUSSION

The results in Figs. 3–6 demonstrate the utility of combining the high-resolution SEVI technique with ion trapping and cryogenic cooling. Before installation of the cryogenic ion trap, typical linewidths of molecular systems were 15–30 cm^{-1} due to rotational broadening.[70–72] Even if there were no spectral congestion from vibrational hot bands and sequence bands, many of the features in the spectra would not have been resolved. For example, peak spacings between peaks L-M and M-N in fluorenyl are only 8 cm^{-1} and 12 cm^{-1}; only peak N would have been apparent in our previous experimental configuration, with an unresolved shoulder at lower energy. Furthermore, depending on the particular system and on source conditions, ion vibrational temperatures have varied from ∼70 to 400 K, resulting in additional sequence bands and spectral congestion. While our previously reported results on SEVI of cryo-cooled ions showed narrowing of the rotational profile and quenching of numerous hot bands, this earlier work was done on simpler systems (C_5^- and S_3^-) with relatively little spectral congestion in the regions of interest.[44,73] Ion trapping and cooling allow for fully vibrationally resolved spectra even for complex polyatomic anions such as indenyl and fluorenyl, which have vibrational activity in numerous modes. The challenge is then to assign the observed structure as completely as possible and to understand the spectral complexities that are revealed at high resolution.

A. Electronic structure

The presence of two well-separated bands in the spectra for each system suggests photodetachment to two different neutral electronic states. The electron configurations of

TABLE III. Calculated electron affinities and term energies compared to experimental results (eV).

		Indenyl	Fluorenyl
B3LYP	EA	1.719	1.809
	T_0	0.942	1.261
CASSCF	T_e	0.796	1.216
	MECI	0.852	1.394
Expt.	EA	1.8019(6)	1.8751(3)
	T_0	0.95(5)	1.257(4)

the closed-shell anions are described by $\ldots(3b_1)^2(2a_2)^2$ for indenyl and $\ldots(3a_2)^2(4b_1)^2$ for fluorenyl; both the HOMO and HOMO-1 are delocalized π-orbitals. Detachment from the HOMO yields the $\tilde{X}^2A_2$ and $\tilde{X}^2B_1$ ground states for indenyl and fluorenyl radicals, respectively, while detachment from the HOMO-1 forms the $\tilde{A}^2B_1$ and $\tilde{A}^2A_2$ excited states. Electronic structure calculations at the B3LYP and CASSCF levels agree on the relative ordering of the neutral states, as listed in Table III. The EOM-IP-CCSD calculations yield the VDEs to these and higher lying neutral states, as listed in Table IV. The calculated VDEs to the neutral ground states are lower than the EAs from B3LYP, likely due to the smaller basis set in the EOM-IP-CCSD calculation not providing sufficient flexibility. The EAs and adiabatic term energies (T_0) calculated by B3LYP are zero-point-vibrational-energy (ZPVE) corrected. As the focus of the CASSCF calculations is on the conical intersection, at which harmonic vibrational frequencies are not meaningful, the excited state term energy (T_e) and MECI energy are not ZPVE-corrected.

The calculated electron affinities and term energies in Table III are in good agreement with the experimental band onsets for indenyl and fluorenyl. The two bands in the anion indenyl photodetachment spectra are thus assigned to the $\tilde{X}^2A_2 \leftarrow \tilde{X}^1A_1$ and $\tilde{A}^2B_1 \leftarrow \tilde{X}^1A_1$ transitions; likewise, those for fluorenyl are assigned to the $\tilde{X}^2B_1 \leftarrow \tilde{X}^1A_1$ and $\tilde{A}^2A_2 \leftarrow \tilde{X}^1A_1$ transitions. Assigning the first peak of each band as the vibrational origin gives electron affinities of indenyl as 1.8019(6) eV and fluorenyl as 1.8751(3) eV. The peaks comprising the excited state bands are broader than the ground states, giving term energies of 0.95(5) eV and 1.257(4) eV, respectively.

Since the detached electrons come from delocalized orbitals, the calculated changes in geometry upon photodetachment are very minor. For detachment to the lowest two neutral states, the calculated CH bond lengths change by at most 0.005 Å, while the CCH bond angles change by less than 1.1°. Larger effects are seen in the carbon ring network. CC bond lengths change by less than 0.05 Å and CCC angles by less than 2°. A full list of the calculated geometries is given in Tables SV and SVI of the supplementary material.[74]

TABLE IV. Calculated vertical detachment energies (VDEs) in eV by EOM–IP–CCSD/6–31+G* from the anion to the indenyl and fluorenyl neutral radicals in the lowest states accessible by one-electron removal in each irreducible representation.

Indenyl		Fluorenyl	
State	VDE	State	VDE
$^2A_2$	1.58	$^2B_1$	1.50
$^2B_1$	2.55	$^2A_2$	2.98
$^2A_1$	6.24	$^2A_1$	6.64
$^2B_2$	7.09	$^2B_2$	6.79

B. Vibrational structure: General considerations

As mentioned in Sec. IV, the experimental spectra taken at various levels of energy resolution show effects beyond simply more structure at higher resolution. In the ground state electronic bands shown in Fig. 2, the FWHM of the origin peaks is 230 cm^{-1} wide, and only partially resolved vibrational structure is seen at higher eBE. Nonetheless, the simulated FC stick spectra match the experimental vibrational profiles reasonably well in the overview spectra. The overview spectra should be at high enough energies that the relative intensities of transitions within the ground state are not influenced by threshold effects.

The medium- and high-resolution fluorenyl ground state spectra also follow the overall shape of the overview spectrum, and many of the peaks in the high-resolution spectra match the position and intensity of features in the FC simulation. However, there are several peaks including C, E, and G that are visible at medium resolution but disappear or lose significant intensity at high resolution, and none of these appear in the FC simulations. In indenyl, the medium-resolution spectrum is strikingly different from the overview. Although the vibrational origin is in the same place, the smaller peaks revealed in this spectrum do not appear to line up with either the overview or with the FC simulation. The high-resolution spectra resolve even more peaks that do not correspond to predicted transitions, and there are features such as peaks D, G, and I that disappear or lose intensity at high resolution.

These effects require a more detailed consideration of the photodetachment process. In the dipole approximation, the intensity of a photodetachment transition is governed by the matrix element $\langle a|\mu|n, e^-\rangle$, which gives the symmetry requirement for photodetachment between anionic and neutral vibronic states $|a\rangle$ and $|n\rangle$,[75–77]

$$\Gamma_a \otimes \Gamma_{\mu_{x,y,z}} \otimes \Gamma_n \otimes \Gamma_{e^-} \supset \Gamma_A. \tag{2}$$

Here, Γ_j is the irreducible representation for the anion state (a), any of the molecule-fixed dipole moments ($\mu_{x,y,z}$), the neutral state (n), the ejected electron (e^-), and the totally symmetric representation (A). In the FC simulations, the Born-Oppenheimer approximation is assumed to hold so that the anion state $|a\rangle = |el_a\rangle\,|v_a\rangle$ and neutral state $|n\rangle = |el_n\rangle\,|v_n\rangle$, i.e., the electronic and vibrational wavefunctions are separable. In addition, the dipole moment operator is assumed to be constant with respect to nuclear geometry. Hence, the intensity of a photodetachment transition is given by

$$I \propto \left|\langle el_a|\,\mu\,\left|el_n, e^-\right\rangle\right|^2 |\langle v_a|\,v_n\rangle|^2\,. \tag{3}$$

The Franck-Condon factor $|\langle v_a|\,v_n\rangle|^2$ places no restrictions on the change in vibrational quantum number Δv for totally symmetric vibrational modes, but odd Δv transitions

in non-totally symmetric vibrational modes will not appear in FC simulations.[76,78,79]

Transitions involving odd quanta of non-symmetric modes can occur if there is vibronic coupling with other electronic states. The most straightforward example is Herzberg-Teller (HT) coupling,[80] in which two neutral electronic states e' and e'' can be coupled by the non-totally symmetric vibrational mode v if

$$\Gamma_{e'} \otimes \Gamma_v \otimes \Gamma_{e''} \supset \Gamma_A, \tag{4}$$

i.e., if the product of the irreducible representations of the two electronic states and the coupling mode contains the totally symmetric representation Γ_A. HT coupling leads to intensity borrowing, in which, for example, the $v = 1$ level of a non-totally symmetric mode in state e'' is mixed with a totally symmetric mode in state e'. Note that in photoionization or photodetachment, the interaction of the molecular core and the outgoing photoelectron can also induce forbidden vibrational transitions without invoking HT coupling, so long as the more general symmetry condition (2) is satisfied.[76,77,81]

An additional consideration is that near-threshold photodetachment cross sections from atomic anions vary with eKE according to the Wigner threshold law,[45]

$$\sigma \propto (\text{eKE})^{\ell+1/2}, \tag{5}$$

where σ is the cross-section and $\ell = 0, 1, 2...$ is the angular momentum of the departing electron. Deviations from Eq. (5) in molecular photodetachment are fairly minor.[82] As a result, the relative intensities of photodetachment transitions at low eKE, where our resolution is highest, can vary markedly depending on the partial wave contributions to the wavefunction $|e^-\rangle$ of the departing electron, which in turn reflect the nature of the anion and neutral electronic states.[75] The PAD also reflects this partial wave decomposition.[83,84]

Assuming no vibronic coupling, s-wave ($\ell = 0$) detachment can occur only if[75]

$$\Gamma_{el_a} \otimes \Gamma_{el_n} \supset \Gamma_{x,y,z}, \tag{6}$$

since the electron scattering wavefunction for an s-wave is isotropic. In C_{2v} symmetry, Eq. (6) implies that s-wave detachment can occur upon detachment from an a_1, b_1, or b_2 orbital. Hence, according to Eq. (5), the cross section near threshold should vary as $\text{eKE}^{1/2}$, and the intensity of these transitions should remain reasonably high at low eKE. In contrast, detachment from an a_2 orbital can only occur by p-wave ($\ell = 1$) and higher order terms, resulting in an $\text{eKE}^{3/2}$ dependence and a much steeper drop in intensity at low eKE.

C. Ground state assignments: Fluorenyl

Assignment of the fluorenyl ground state vibrations is reasonably straightforward. Both the low- and high-resolution spectra qualitatively match the FC simulation. As shown in Fig. 5, good agreement with experiment and simulation enables assignment of most peaks. Table II shows that peaks B, D, E, I, N, R, S, V, Y, Z, and AA agree with simulated relative intensities and positions for various fundamentals of totally symmetric a_1 vibrational modes. Peaks L, W, AB, and AC are active in the FC simulation as combination bands. The maximum offset between calculated and experimental positions is only 7 cm^{-1}. All of these transitions are fully FC-allowed. Additional peaks are close to calculated vibrational frequencies, but the presence of non-FC-allowed peaks (see below) along with spectral congestion makes further assignments questionable. Unsurprisingly, as the most significant geometry changes are in the carbon ring network, most of the FC activity is in various in-plane ring-deformation modes. Comparison of the blue and black traces in Fig. 5 indicates that all peaks listed above maintain similar relative intensities at medium and high resolution.

Of the remaining peaks, the positions of C, E, and G line up with the calculated fundamentals of three vibrational modes with b_1 symmetry. These three peaks deviate by at most 7 cm^{-1} from the calculated fundamentals of the b_1 modes ν_{39}, ν_{37}, and ν_{36}, respectively, and all nearby a_1 modes are already accounted for. Peaks E and G also have a PAD with positive β, in contrast to all other transitions. Peak C may as well, though low signal-to-noise prevents an unambiguous evaluation of its PAD. The intensities of all three peaks are lower at high resolution than at medium resolution, and none of them appear in the FC simulation. The absence of these peaks in the simulation is not surprising, since all involve $\Delta v = 1$ transitions in a non-totally symmetric (b_1) vibrational mode. The more interesting question is why they appear at all, and why their intensities and PADs differ from those of the fully allowed FC transitions.

According to Eq. (4), a b_1 vibrational mode in a B_1 electronic state can be activated through HT coupling to an excited state with A_1 symmetry. The lowest $^2A_1$ state accessible by one-electron detachment is calculated to lie 5.1 eV above the ground state by EOM-IP-CCSD, or 3.85–4.77 eV by TDDFT.[63] The PADs for peaks C, E, and G, characterized by positive β, are consistent with coupling to this state. In the s&p model developed by Surber *et al.*,[84] the PAD is qualitatively determined by taking the symmetry-allowed character of the detached electron and expanding it as a combination of molecule-centered s- and p-wave electrons. Due to the Wigner threshold law, higher order partial waves are assumed to be of minor significance near threshold. In this model, for a C_{2v}-symmetric system, a positive β comes from photodetachment of an electron from an a_1 orbital and a negative-to-zero β by detachment from an a_2, b_1, or b_2 orbital. Detachment from an a_1 orbital in a closed-shell anion leads to a $^2A_1$ neutral state. If peaks C, E, and G borrow intensity from the $^2A_1$ excited state, they will also borrow its electronic character and thus have a positive β PAD, as seen experimentally.[85] Although it is surprising to see evidence of coupling to such a high-lying state, the positive β values argue against coupling to a state with symmetry other than A_1. Similar effects of HT coupling on the PAD have been seen in previous photoelectron and SEVI spectra of C_2H^- and other anions.[72,86,87]

One also might expect to see HT coupling with the $\tilde{A}^2A_2$ state, as this state lies only 1.26 eV above the ground state of fluorenyl. This coupling would activate vibrational modes of b_2 symmetry in the ground state spectrum, but no such modes are identified in Table II. The absence of such features may reflect the consequences of the Wigner threshold

law. According to Eq. (6), s-wave detachment to the fluorenyl ground state can occur as this involves electron ejection from a b_2 orbital. In contrast, the $\tilde{A}^2A_2$ state is accessed by ejection of an electron in an a_2 orbital and should thus involve p-wave detachment to lowest order. For transitions allowed only by intensity-borrowing from an excited electronic state, the symmetry of this state should be used in Eq. (6). As a result, the near-threshold cross section for $\Delta v = 1$ transitions in b_2 vibrations should vary as $\text{eKE}^{3/2}$ and the corresponding peaks will be discriminated against in high-resolution SEVI scans.

Note that according to the above arguments, peaks C, E, and G, which have been attributed to coupling to an excited $^2A_1$ state, should also be accessible via s-wave detachment. However, their intensities fall off more quickly at low eKE compared to the fully allowed transitions. While s-wave contributions are symmetry-allowed, the actual partial wave decomposition for these features may well involve greater contributions from higher-ℓ components because a different neutral electronic state is involved. The observation of a subset of peaks with a different intensity dependence on eKE than the fully allowed transitions provides an additional signature of vibronic coupling, but the nature of this dependence may be difficult to predict *a priori*.

D. Ground state assignments: Indenyl

The indenyl SEVI spectrum, at first glance, resembles the fluorenyl spectrum, as both are dominated by the vibrational origin (peak A) followed by many smaller transitions at higher eBE to vibrationally excited states of the neutral. This overall appearance reflects the fact that neither anion undergoes much of a geometry change upon photodetachment to the neutral ground state. However, as discussed above, the relative intensity distribution is more sensitive to eKE in indenyl. While the fluorenyl ground-state spectra can be largely assigned through the FC simulation, agreement between the high-resolution indenyl spectra and FC simulations is considerably worse.

Comparison of the experimental and calculated frequencies in Table I shows that virtually all of the higher eBE peaks in the medium- and high-resolution indenyl spectra that can be assigned correspond to $\Delta v = 1$ transitions in non-totally symmetric modes. Since no modes are expected to have a frequency below 233 cm^{-1} (see Table SV in the supplementary material[74]) and there are no periodic spacings indicative of combination bands, the observed vibrational structure should be dominated by $\Delta v = 1$ transitions up to $\sim$800 cm^{-1}. Only three a_1 modes have calculated frequencies below 1000 cm^{-1} and none of the FC calculated transitions matches in position and intensity, so all assigned peaks are the best-matched fundamentals of non-totally symmetric modes. Typical discrepancies between experimental and calculated frequencies are less than 4 cm^{-1}. Since these transitions are not FC-allowed, they do not appear in the FC simulations. The question then is why these spectra appear to be dominated by vibronically allowed transitions, in contrast to fluorenyl, and why the simulated FC-allowed transitions generally do not line up with experimental peaks.

The key differences between the indenyl and fluorenyl spectra arise because the $^2A_2$ ground state of indenyl is accessed by photodetachment from an a_2 orbital. Hence, near threshold, $\tilde{X}^2A_2 \leftarrow \tilde{X}^1A_1$ photodetachment should be p-wave, with a cross section proportional to $\text{eKE}^{3/2}$. One manifestation of p-wave detachment is seen in the intense origin peak. Although it is the dominant feature in the indenyl overview scan, its intensity diminishes dramatically as the photon energy is reduced. It was necessary to take a scan $\sim$100 cm^{-1} above the peak center for acceptable signal at high resolution, resulting in a peak FWHM of 11 cm^{-1}. In contrast, as can be seen by comparing Figs. 3 and 5, we were able to acquire a $\sim$5 cm^{-1} wide peak of the fluorenyl origin with the laser only 20 cm^{-1} above threshold. That scan took an order of magnitude less time than the indenyl origin scan even though the ion signals and laser pulse energies were similar. Moreover, in comparing the EAs from our experiment with those obtained in total cross section measurements by Römer *et al.*,[40] we find that our EA of fluorenyl lies within their error bars, at 1.8751(3) compared to 1.864(14) eV. However, at 1.8019(6) eV, our indenyl EA is 50 meV lower than their reported value of 1.853(14) eV and outside of their given error bounds. This discrepancy most likely reflects the difficulty in extracting the EA from a total cross section measurement in which p-wave detachment dominates, owing to the very slow rise in the cross section above the EA.

The smaller peaks in the indenyl spectrum are also affected by these considerations. Transitions involving excitation of totally symmetric vibrational levels will also exhibit an $\text{eKE}^{3/2}$ intensity dependence. Hence these transitions, which typically dominate a photoelectron spectrum, will be discriminated against at high resolution. In contrast, $\Delta v = 1$ transitions in a_2, b_1, or b_2 vibrational modes can occur via Herzberg-Teller coupling to A_1, B_2, or B_1 excited states, respectively, which allows s-wave detachment in all three cases. We were able to obtain higher resolution spectra (6–9 cm^{-1}) of these peaks than of the much more intense origin peak, because they could be scanned at lower eKE, typically 30–80 cm^{-1}, without an accompanying drop in intensity.

The overall trends in the indenyl spectra with increasing resolution can now be understood. At low resolution (Fig. 2), where the eKE is relatively high, the spectrum is most likely dominated by transitions to totally symmetric vibrational levels, even though the individual levels cannot be resolved. As a result, the FC simulations match the spectral envelope reasonably well. At progressively higher-resolution scans, the FC-allowed transitions lose intensity relative to the HT-allowed transitions, leading to the observed spectral shifting and increasingly poorer agreement between experimental and simulated spectra.

Examining the assigned peaks in more detail, we see that peaks D, G, and I, all assigned to a_2 fundamentals, are the only peaks whose PADs exhibit positive values of β. As was the case in fluorenyl, the peak assignments and PADs are consistent with vibronic coupling to an excited $^2A_1$ state. Peaks E, J, O, P, R, and T are assigned to $\Delta v = 1$ transitions in b_2 modes. These transitions are allowed by Herzberg-Teller coupling with the low-lying $\tilde{A}\ ^2B_1$ ($T_0 = 0.95$ eV) state seen

experimentally in Figs. 2 and 4. Additional evidence for coupling between the $\tilde{X}$ and $\tilde{A}$ states is presented in Sec. V E.

Peaks C, F, and H lie very close to calculated $\Delta v = 1$ transitions in b_1 modes, which are allowed by coupling to a $^2B_2$ excited state. The lowest lying state with this symmetry is calculated to be approximately 5.5 eV above the ground state (see Table IV). This energy spacing might seem rather high for HT coupling, which should diminish as the energy gap between the coupled electronic states increases, and one must consider if mechanisms other than HT coupling are operative.[77] On the other hand, all of these vibronically allowed transitions are quite weak. The intensity of peak C, for example, is only 10% that of the origin transition in the medium-resolution spectrum shown in Fig. 3. Since the intensity of the origin band is reduced by threshold effects in the medium-resolution scan, the true relative intensities of the HT-allowed transitions are even smaller, and the FC-allowed transitions which dominate in the overview spectra are not seen. The intensities of the forbidden transitions should also scale roughly with the mixing of the diabatic states, which is equal to the ratio of the interstate coupling constant divided by the difference in energies between the states.[88] The ratio of gaps to the $^2B_2$ and $^2B_1$ states is ∼5. Assuming similar coupling strengths, the intensities of the corresponding vibronically allowed peaks should be within an order of magnitude of each other.

As has been done in other photodetachment experiments, a detailed vibronic coupling calculation could resolve the question of which states couple with each other along which modes, and a simulated spectrum could be compared with experiment for further validation.[89–95] However, such a calculation is beyond the scope of this paper.

The above discussion of vibronic coupling depends on our ability to assign the large number of active vibrational modes correctly on the basis of comparison to calculated harmonic vibrational frequencies. Relaxation of the FC requirement allows for many more possible ways to assign peaks incorrectly; in light of this, the peak assignments were done conservatively. For the FC-allowed transitions, peaks were only assigned when their positions and intensities matched simulation. The FC-forbidden transitions were only assigned when the PAD and vibrational frequency were consistent with the proposed coupling, or in a few rare cases where no other likely possibilities remained. Furthermore, though vibronic coupling perturbs the potential energy surface of the ground state, the spectra are taken well below any conical intersections and relatively weak couplings at the large energy separations here give only minimal nonadiabatic contributions to the vibrational frequencies.[88]

E. Excited state assignments and dynamics

Although the spectra of the excited state bands were taken under identical experimental conditions as the ground state bands, the excited state peaks are considerably wider. As shown in Fig. 6, the fluorenyl $\tilde{A}^2A_2 \leftarrow \tilde{X}^1A_1$ band looks qualitatively like the FC simulation. The major FC-active transitions in the simulation are 0_0^0, 20_0^1, 18_0^1, 20_0^2, $18_0^120_0^1$, and 9_0^1. The match is quite good to peaks a–f of the fluorenyl excited state in position and relative intensity, so they are assigned accordingly. Since the detached electron comes from a π-orbital, FC activity is mainly in ring deformation motions, similar to the ground state. As was the case for detachment to the indenyl $\tilde{X}\,^2A_2$ state, the cross-section diminished rapidly near threshold and scans were only taken down to 220 cm^{-1} above threshold. However, at similar eKE, peaks in the indenyl ground state band exhibited widths of 14 cm^{-1}, while fluorenyl excited state peak widths remained above 55 cm^{-1}. Assuming the instrumental resolution and intrinsic peak widths are independent, this gives an intrinsic linewidth of 53 cm^{-1}.

The indenyl $\tilde{A}^2B_1 \leftarrow \tilde{X}^1A_1$ band has no discernible vibrational structure, even in a higher resolution scan closer to threshold (Fig. 4). Although the simulation predicts minor FC activity with the origin as the major peak, we observe only a single, broad feature with a FWHM of 930 cm^{-1}, which can be approximately fit by assigning a width of 800 cm^{-1} to the peaks in the FC simulation.

The large peak widths of the indenyl and fluorenyl excited state bands cannot be from spectral congestion within the excited states, since the FC simulations show relatively little vibrational activity and nearby ground state features taken under the same experimental conditions are much narrower. They are instead suggestive of a fast decay mechanism in the $\tilde{A}$ states of both species. Assuming a monoexponential decay, we can apply the standard formula $\tau = 1/(2\pi\Gamma)$, where τ is the characteristic time constant and Γ is the FWHM. The peak widths thus correspond to lifetimes of 7 fs and 100 fs, respectively, for the $\tilde{A}^2B_1$ indenyl and $\tilde{A}^2A_2$ fluorenyl excited states. The indenyl $\tilde{A}^2B_1$ spectra are not vibrationally resolved, so the 7 fs lifetime estimate assumes that the FC simulation is a reasonable zero-order model for photodetachment to the $\tilde{A}^2B_1$ state. The excited states lie well below the lowest dissociation limit for either radical, and the lifetimes from the peak widths are clearly too short to be from radiative decay. It is therefore reasonable to attribute them to very fast non-radiative decay to the $\tilde{X}$ states, most likely due to low-lying conical intersections.[96,97]

Similar line-broadening effects have been observed in the electronic spectra of the π-isoelectronic naphthalene[98,99] and anthracene[100] cations and, at lower resolution, in excited state bands in the photoelectron spectra of naphthalene and anthracene.[101,102] Electronic structure calculations by Hall *et al.*[103] and Ghanta *et al.*[104] have identified low-lying conical intersections between the $\tilde{X}$, $\tilde{A}$, and $\tilde{B}$ states of the cations. Quantum dynamics calculations[105] show that these conical intersections lead to non-radiative decay lifetimes ranging from 20 to 225 fs out of the $\tilde{A}$ and $\tilde{B}$ states of the naphthalene and anthracene cations.

To investigate the feasibility of a similar mechanism for the low-lying excited states of indenyl and fluorenyl, we carried out electronic structure calculations as described in Sec. III to determine the energies of the $\tilde{X} - \tilde{A}$ minimum energy conical intersections compared to the $\tilde{X}$ and $\tilde{A}$ equilibrium geometries. The energies are listed in Table III, and schematic cuts through the potential energy surfaces are shown in Fig. 7. The tuning coordinate primarily involves changes along the in-plane CC bond lengths and CCC bond

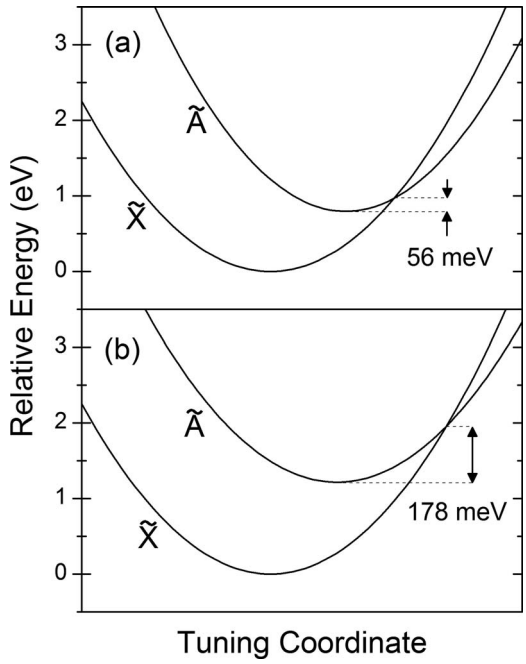

FIG. 7. Schematic diagram of the intersecting potential energy curves of the two lowest electronic states of indenyl (a) and fluorenyl (b).

angles, similar to the changes in equilibrium geometries between the anion and neutral states. A full list of calculated geometries is given in Tables SIII and SIV of the supplementary information.[74] No single vibrational mode is a dominant component of the tuning coordinate, so it is left unlabeled as a qualitative guide. Despite the lack of dynamical correlation in the CASSCF treatment and the relatively small basis set used, the relative energies of the lowest lying states are in good agreement with the DFT calculations and with the experimental results. Therefore, this level of theory is expected to treat the energetics near the first conical intersection reasonably accurately.

We find that the indenyl and fluorenyl neutral species have low-lying conical intersections connecting their $\tilde{X}$ and $\tilde{A}$ states. Our calculations suggest that the MECIs are only 56 meV and 178 meV above the respective $\tilde{A}$ state minima. As the fluorenyl $\tilde{X} - \tilde{A}$ MECI lies higher above the $\tilde{A}$ state minimum than in indenyl, low-lying vibrational levels of the fluorenyl $\tilde{A}$ state should be less perturbed by the conical intersection, and are thus expected to decay more slowly. Such a conclusion would be consistent with the dynamics calculations by Ghanta *et al.*,[105] who calculated naphthalene and anthracene cation $\tilde{A}$ state lifetimes of 20 and 225 fs, with the corresponding MECIs lying 110 and 720 meV above the excited state minima. Given these results, the short lifetimes inferred for fluorenyl and indenyl from line-broadening appear to be reasonable, as is the faster decay for indenyl.

Similar effects have been seen in other photoelectron spectra. A spectrum of the pyrrolide anion exhibited a partially vibrationally resolved transition to the ground state, but a featureless broad spectrum for the excited state.[42] The authors estimated that the MECI was only 10 meV above the $\tilde{A}$ state saddle point, and attributed the broad feature to fast relaxation through the $\tilde{X} - \tilde{A}$ conical intersection. A more sophisticated MRCI treatment was later used to calculate an energy difference of 16 meV, and was also used for a sophisticated multimode vibronic coupling simulation of the spectra, which confirmed a featureless broad transition to the excited state.[93]

The broadening observed for the first excited states raises the possibility that there is little gas-phase spectroscopic work on these species partly because of fast non-radiative decay mechanisms. The work by Ghanta *et al.*[104] suggests that the higher excited states of indenyl and fluorenyl may also undergo fast internal conversion. These would interfere with the most popular action spectroscopy techniques used on radicals, laser-induced fluorescence, and resonant multiphoton ionization, as they would quench fluorescence and reduce ionization yield.[106,107] We note that higher lying C_9H_7 isomers 1-phenylpropargyl and 3-phenylpropargyl have been observed with fluorescence and multiphoton ionization techniques,[108–110] as has the bicyclic 1-indanyl radical (C_9H_9), which is structurally similar to indenyl but has one fewer double bond.[111] It would thus be of considerable interest to investigate the role of conical intersections in the dynamics and spectroscopy of these radicals and compare them to indenyl and fluorenyl.

VI. CONCLUSIONS

High-resolution photoelectron spectra, obtained by combining SEVI spectroscopy with ion trapping and cryogenic cooling, are reported for the indenyl and fluorenyl anions. More accurate values are reported for the electron affinities of the neutral radicals, and term energies are reported for the first excited states, which have not been observed before experimentally. Numerous vibrational frequencies have been determined for the first time, including those of many non-totally symmetric modes. While the indenyl ground state spectra show excitation largely in non-totally symmetric modes through vibronic coupling, the fluorenyl spectra largely follow the FC simulation. These differences are attributed to a combination of vibronic coupling and threshold photodetachment effects. Broad linewidths of the excited states suggest strong nonadiabatic coupling with the ground state, with a fast non-radiative decay from the first excited states via low-lying conical intersections. Similar vibronic coupling and conical intersection dynamics are expected to be important for other radical polycyclic aromatic systems.

ACKNOWLEDGMENTS

This research is funded by the Air Force Office of Scientific Research under Grant No. FA9550-12-1-0160 and the Defense University Research Instrumentation Program under Grant No. FA9550-11-1-0300. M.L.W. thanks the National Science Foundation for a graduate research fellowship.

[1]M. F. Denissenko, A. Pao, M.-S. Tang, and G. P. Pfeifer, Science **274**, 430 (1996).
[2]H. Richter and J. B. Howard, Prog. Energ. Combust. Sci. **26**, 565 (2000).
[3]S. A. Skeen, H. A. Michelsen, K. R. Wilson, D. M. Popolan, A. Violi, and N. Hansen, J. Aerosol Sci. **58**, 86 (2013).
[4]A. G. G. M. Tielens, Rev. Mod. Phys. **85**, 1021 (2013).

[5]L. J. Allamandola, A. Tielens, and J. R. Barker, Astrophys. J. Suppl. Ser. **71**, 733 (1989).
[6]L. J. Allamandola, D. M. Hudgins, and S. A. Sandford, Astrophys. J. **511**, L115 (1999).
[7]A. Tielens, Annu. Rev. Astron. Astrophys. **46**, 289 (2008).
[8]T. P. Snow, Spectrochim. Acta A **57**, 615 (2001).
[9]T. P. Snow and B. J. McCall, Annu. Rev. Astron. Astrophys. **44**, 367 (2006).
[10]I. Cherchneff, J. R. Barker, and A. Tielens, Astrophys. J. **401**, 269 (1992).
[11]A. P. Jones, A. Tielens, and D. J. Hollenbach, Astrophys. J. **469**, 740 (1996).
[12]D. Teyssier, D. Fossé, M. Gerin, J. Pety, A. Abergel, and E. Roueff, Astron. Astrophys. **417**, 135 (2004).
[13]J. Pety, D. Teyssier, D. Fossé, M. Gerin, E. Roueff, A. Abergel, E. Habart, and J. Cernicharo, Astron. Astrophys. **435**, 885 (2005).
[14]M. Frenklach and L. B. Ebert, J. Phys. Chem. **92**, 561 (1988).
[15]H. Guesten, L. Klasinc, and B. Ruscic, Z. Naturforsch. A **31A**, 1051 (1976).
[16]S. H. Reza Shojaei, F. Morini, and M. S. Deleuze, Chem. Phys. **417**, 17 (2013).
[17]C. Qin, S. Y. Tzeng, B. Zhang, and W. B. Tzeng, J. Photochem. Photobiol. A **220**, 139 (2011).
[18]X. Zhang, J. D. Pitts, R. Nadarajah, and J. L. Knee, J. Chem. Phys. **107**, 8239 (1997).
[19]G. D. Silva and J. W. Bozzelli, J. Phys. Chem. A **113**, 8971 (2009).
[20]S. Fascella, C. Cavallotti, R. Rota, and S. Carrà, J. Phys. Chem. A **109**, 7546 (2005).
[21]S. Granata, T. Faravelli, E. Ranzi, N. Olten, and S. Senkan, Combust. Flame **131**, 273 (2002).
[22]L. Vereecken and J. Peeters, Phys. Chem. Chem. Phys. **5**, 2807 (2003).
[23]A. Matsugi and A. Miyoshi, Phys. Chem. Chem. Phys. **14**, 9722 (2012).
[24]N. M. Marinov, M. J. Castaldi, C. F. Melius, and W. Tsang, Combust. Sci. Tech. **128**, 295 (1997).
[25]C.-W. Zhou, V. V. Kislov, and A. M. Mebel, J. Phys. Chem. A **116**, 1571 (2012).
[26]M. Tian, B. S. Liu, M. Hammonds, N. Wang, P. J. Sarre, and A. S. C. Cheung, Phys. Chem. Chem. Phys. **14**, 6603 (2012).
[27]L. Vereecken, J. Peeters, H. F. Bettinger, R. I. Kaiser, P. V. R. Schleyer, and H. F. Schaefer, J. Am. Chem. Soc. **124**, 2781 (2002).
[28]D. S. N. Parker, F. Zhang, R. I. Kaiser, V. V. Kislov, and A. M. Mebel, Chem. Asian J. **6**, 3035 (2011).
[29]F. Zhang, R. I. Kaiser, V. V. Kislov, A. M. Mebel, A. Golan, and M. Ahmed, J. Phys. Chem. Lett. **2**, 1731 (2011).
[30]B. Shukla, A. Susa, A. Miyoshi, and M. Koshi, J. Phys. Chem. A **111**, 8308 (2007).
[31]B. Shukla, A. Susa, A. Miyoshi, and M. Koshi, J. Phys. Chem. A **112**, 2362 (2008).
[32]A. Matsugi and A. Miyoshi, Proc. Combust. Inst. **34**, 269 (2013).
[33]C. Cavallotti, S. Mancarella, R. Rota, and S. Carrà, J. Phys. Chem. A **111**, 3959 (2007).
[34]A. Atto, A. Hudson, R. A. Jackson, and N. P. C. Simmons, Chem. Phys. Lett. **33**, 477 (1975).
[35]R. Livingston, H. Zeldes, and M. S. Conradi, J. Am. Chem. Soc. **101**, 4312 (1979).
[36]P. Hemberger, M. Steinbauer, M. Schneider, I. Fischer, M. Johnson, A. Bodi, and T. Gerber, J. Phys. Chem. A **114**, 4698 (2010).
[37]M. Lang, F. Holzmeier, I. Fischer, and P. Hemberger, J. Phys. Chem. A **117**, 5260 (2013).
[38]T. Izumida, K. Inoue, S. Noda, and H. Yoshida, Bull. Chem. Soc. Jpn. **54**, 2517 (1981).
[39]J. Szczepanski, J. Banisaukas, M. Vala, S. Hirata, and W. R. Wiley, J. Phys. Chem. A **106**, 6935 (2002).
[40]B. Römer, G. A. Janaway, and J. I. Brauman, J. Am. Chem. Soc. **119**, 2249 (1997).
[41]P. C. Engelking and W. C. Lineberger, J. Chem. Phys. **67**, 1412 (1977).
[42]A. J. Gianola, T. Ichino, R. L. Hoenigman, S. Kato, V. M. Bierbaum, and W. C. Lineberger, J. Phys. Chem. A **108**, 10326 (2004).
[43]T. Ichino, S. W. Wren, K. M. Vogelhuber, A. J. Gianola, W. C. Lineberger, and J. F. Stanton, J. Chem. Phys. **129**, 084310 (2008).
[44]C. Hock, J. B. Kim, M. L. Weichman, T. I. Yacovitch, and D. M. Neumark, J. Chem. Phys. **137**, 244201 (2012).
[45]E. P. Wigner, Phys. Rev. **73**, 1002 (1948).
[46]D. M. Neumark, J. Phys. Chem. A **112**, 13287 (2008).
[47]A. Osterwalder, M. J. Nee, J. Zhou, and D. M. Neumark, J. Chem. Phys. **121**, 6317 (2004).
[48]A. Eppink and D. H. Parker, Rev. Sci. Instrum. **68**, 3477 (1997).
[49]U. Even, J. Jortner, D. Noy, N. Lavie, and C. Cossart-Magos, J. Chem. Phys. **112**, 8068 (2000).
[50]M. B. Doyle, C. Abeyasera, and A. G. Suits, computer program NuACQ, see http://chem.wayne.edu/suitsgroup/NuACQ.html.
[51]E. W. Hansen and P.-L. Law, J. Opt. Soc. Am. A **2**, 510 (1985).
[52]C. Blondel, W. Chaibi, C. Delsart, C. Drag, F. Goldfarb, and S. Kröger, Eur. Phys. J. D **33**, 335 (2005).
[53]U. Berzinsh, M. Gustafsson, D. Hanstorp, A. Klinkmüller, U. Ljungblad, and A. M. Mårtensson-Pendrill, Phys. Rev. A **51**, 231 (1995).
[54]J. Cooper and R. N. Zare, J. Chem. Phys. **48**, 942 (1968).
[55]C. Bartels, C. Hock, J. Huwer, R. Kuhnen, J. Schwöbel and B. von Issendorff, Science **323**, 1323 (2009).
[56]R. Mabbs, E. R. Grumbling, K. Pichugin, and A. Sanov, Chem. Soc. Rev. **38**, 2169 (2009).
[57]M. J. Nee, A. Osterwalder, J. Zhou, and D. M. Neumark, J. Chem. Phys. **125**, 014306 (2006).
[58]C. M. Oana and A. I. Krylov, J. Chem. Phys. **131**, 124114 (2009).
[59]A. T. B. Gilbert, N. A. Besley, and P. M. W. Gill, J. Phys. Chem. A **112**, 13164 (2008).
[60]J. Simons, J. Phys. Chem. A **112**, 6401 (2008).
[61]D. Sinha, S. K. Mukhopadhyay, R. Chaudhuri, and D. Mukherjee, Chem. Phys. Lett. **154**, 544 (1989).
[62]A. I. Krylov, Annu. Rev. Phys. Chem. **59**, 433 (2008).
[63]J. Szczepanski, J. Banisaukas, M. Vala, S. Hirata, R. J. Bartlett, and M. Head-Gordon, J. Phys. Chem. A **106**, 63 (2002).
[64]Y. Shao, L. F. Molnar, Y. Jung, J. Kussmann, C. Ochsenfeld, S. T. Brown, A. T. B. Gilbert, L. V. Slipchenko, S. V. Levchenko, D. P. O'Neill, R. A. DiStasio, Jr., R. C. Lochan, T. Wang, G. J. O. Beran, N. A. Besley, J. M. Herbert, C. Yeh Lin, T. Van Voorhis, S. Hung Chien, A. Sodt, R. P. Steele, V. A. Rassolov, P. E. Maslen, P. P. Korambath, R. D. Adamson, B. Austin, J. Baker, E. F. C. Byrd, H. Dachsel, R. J. Doerksen, A. Dreuw, B. D. Dunietz, A. D. Dutoi, T. R. Furlani, S. R. Gwaltney, A. Heyden, S. Hirata, C.-P. Hsu, G. Kedziora, R. Z. Khalliulin, P. Klunzinger, A. M. Lee, M. S. Lee, W. Liang, I. Lotan, N. Nair, B. Peters, E. I. Proynov, P. A. Pieniazek, Y. Min Rhee, J. Ritchie, E. Rosta, C. David Sherrill, A. C. Simmonett, J. E. Subotnik, H. Lee Woodcock III, W. Zhang, A. T. Bell, A. K. Chakraborty, D. M. Chipman, F. J. Keil, A. Warshel, W. J. Hehre, H. F. Schaefer III, J. Kong, A. I. Krylov, P. M. W. Gill, and M. Head-Gordon, Phys. Chem. Chem. Phys. **8**, 3172 (2006).
[65]H.-J. Werner, P. J. Knowles, G. Knizia, F. R. Manby, M. Schütz *et al.*, MOLPRO, version 2010.1, a package of *ab initio* programs, see http://www.molpro.net
[66]R. S. Mulliken, J. Chem. Phys. **23**, 1997 (1955).
[67]V. A. Mozhayskiy, and A. I. Krylov, computer program ezSpectrum, see http://iopenshell.usc.edu/downloads.
[68]F. Duschinsky, Acta Physicochim. URSS **7**, 551 (1937).
[69]S. Rashev, Int. J. Quantum Chem. **99**, 894 (2004).
[70]J. B. Kim, T. I. Yacovitch, C. Hock, and D. M. Neumark, Phys. Chem. Chem. Phys. **13**, 17378 (2011).
[71]E. Garand, T. I. Yacovitch, and D. M. Neumark, J. Chem. Phys. **129**, 074312 (2008).
[72]T. I. Yacovitch, J. B. Kim, E. Garand, D. G. van der Poll, and D. M. Neumark, J. Chem. Phys. **134**, 134307 (2011).
[73]J. B. Kim, C. Hock, T. I. Yacovitch, and D. M. Neumark, J. Phys. Chem. A **117**, 8126 (2013).
[74]See supplementary material at http://dx.doi.org/10.1063/1.4820138 for calculated geometries of all species and vibrational frequencies of the neutral ground states.
[75]K. J. Reed, A. H. Zimmerman, H. C. Andersen, and J. I. Brauman, J. Chem. Phys. **64**, 1368 (1976).
[76]M. C. R. Cockett, H. Ozeki, K. Okuyama, and K. Kimura, J. Chem. Phys. **98**, 7763 (1993).
[77]G. J. Rathbone, E. D. Poliakoff, J. D. Bozek, and R. R. Lucchese, Can. J. Chem. **82**, 1043 (2004).
[78]K. M. Ervin, J. Ho, and W. C. Lineberger, J. Chem. Phys. **91**, 5974 (1989).
[79]A. Weaver, D. W. Arnold, S. E. Bradforth, and D. M. Neumark, J. Chem. Phys. **94**, 1740 (1991).
[80]G. J. Small, J. Chem. Phys. **54**, 3300 (1971).
[81]S. Han and D. R. Yarkony, Mol. Phys. **110**, 845 (2012).

[82]P. A. Schulz, R. D. Mead, P. L. Jones, and W. C. Lineberger, J. Chem. Phys. **77**, 1153 (1982).
[83]K. L. Reid, Annu. Rev. Phys. Chem. **54**, 397 (2003).
[84]E. Surber, R. Mabbs, and A. Sanov, J. Phys. Chem. A **107**, 8215 (2003).
[85]P. Roy, R. J. Bartlett, W. J. Trela, T. A. Ferrett, A. C. Parr, S. H. Southworth, J. E. Hardis, V. Schmidt, and J. L. Dehmer, J. Chem. Phys. **94**, 949 (1991).
[86]K. M. Ervin and W. C. Lineberger, J. Phys. Chem. **95**, 1167 (1991).
[87]J. Zhou, E. Garand, and D. M. Neumark, J. Chem. Phys. **127**, 114313 (2007).
[88]J. F. Stanton, J. Chem. Phys. **133**, 174309 (2010).
[89]M. Mayer, L. S. Cederbaum, and H. Köppel, J. Chem. Phys. **100**, 899 (1994).
[90]K. R. Asmis, T. R. Taylor, and D. M. Neumark, J. Chem. Phys. **111**, 8838 (1999).
[91]E. Garand, K. Klein, J. F. Stanton, J. Zhou, T. I. Yacovitch, and D. M. Neumark, J. Phys. Chem. A **114**, 1374 (2010).
[92]B. N. Papas, M. S. Schuurman, and D. R. Yarkony, J. Chem. Phys. **130**, 064306 (2009).
[93]X. L. Zhu and D. R. Yarkony, J. Phys. Chem. C **114**, 5312 (2010).
[94]K. Klein, E. Garand, T. Ichino, D. Neumark, J. Gauss, and J. Stanton, Theor. Chem. Acc. **129**, 527 (2011).
[95]C. S. Simmons, T. Ichino, and J. F. Stanton, J. Phys. Chem. Lett. **3**, 1946 (2012).
[96]W. Domcke and D. R. Yarkony, Annu. Rev. Phys. Chem. **63**, 325 (2012).
[97]H. Köppel, W. Domcke, and L. S. Cederbaum, *Advances in Chemical Physics* (John Wiley & Sons, Inc., 1984), Vol. 57, pp. 59–246.
[98]T. Pino, N. Boudin, and P. Brechignac, J. Chem. Phys. **111**, 7337 (1999).
[99]L. Biennier, F. Salama, L. J. Allamandola, and J. J. Scherer, J. Chem. Phys. **118**, 7863 (2003).
[100]O. Sukhorukov, A. Staicu, E. Diegel, G. Rouillé, T. Henning, and F. Huisken, Chem. Phys. Lett. **386**, 259 (2004).
[101]R. S. Sánchez-Carrera, V. Coropceanu, D. A. da Silva Filho, R. Friedlein, W. Osikowicz, R. Murdey, C. Suess, W. R. Salaneck, and J.-L. Brédas, J. Phys. Chem. B **110**, 18904 (2006).
[102]D. A. da Silva Filho, R. Friedlein, V. Coropceanu, G. Ohrwall, W. Osikowicz, C. Suess, S. L. Sorensen, S. Svensson, W. R. Salaneck, and J.-L. Bredas, Chem. Commun., **2004**, 1702.
[103]K. F. Hall, M. Boggio-Pasqua, M. J. Bearpark, and M. A. Robb, J. Phys. Chem. A **110**, 13591 (2006).
[104]S. Ghanta, V. S. Reddy, and S. Mahapatra, Phys. Chem. Chem. Phys. **13**, 14524 (2011).
[105]S. Ghanta, V. S. Reddy, and S. Mahapatra, Phys. Chem. Chem. Phys. **13**, 14531 (2011).
[106]T. A. Miller, Mol. Phys. **104**, 2581 (2006).
[107]N. Chalyavi, T. P. Troy, M. Nakajima, B. A. Gibson, K. Nauta, R. G. Sharp, S. H. Kable, and T. W. Schmidt, J. Phys. Chem. A **115**, 7959 (2011).
[108]N. J. Reilly, D. L. Kokkin, M. Nakajima, K. Nauta, S. H. Kable, and T. W. Schmidt, J. Am. Chem. Soc. **130**, 3137 (2008).
[109]N. J. Reilly, M. Nakajima, B. A. Gibson, T. W. Schmidt, and S. H. Kable, J. Chem. Phys. **130**, 144313 (2009).
[110]K. H. Fischer, J. Herterich, I. Fischer, S. Jaeqx, and A. M. Rijs, J. Phys. Chem. A **116**, 8515 (2012).
[111]T. P. Troy, M. Nakajima, N. Chalyavi, R. L. G. C. R. Clady, K. Nauta, S. H. Kable, and T. W. Schmidt, J. Phys. Chem. A **113**, 10279 (2009).